ENGINEERING

Nanoparticle contact printing with interfacial engineering for deterministic integration into functional structures

Weikun Zhu[1], Peter F. Satterthwaite[2], Patricia Jastrzebska-Perfect[2], Roberto Brenes[2], Farnaz Niroui[2]*

Deterministic, pristine, and scalable integration of individual nanoparticles onto arbitrary surfaces is an ongoing challenge, yet essential for harnessing their unique properties for functional nanoscale devices. To address this challenge, we present a versatile technique where spatially arranged nanoparticles assembled in a topographical template are printed onto diverse surfaces, through a single contact-and-release step, with >95% transfer yield and <50-nanometer placement accuracy. Through engineering of interfacial interactions, our approach uniquely promotes high-yield transfer of individual particles without needing solvents, surface treatments, and polymer sacrificial layers, which are conventionally inevitable. By avoiding these mediation steps, surfaces can remain damage and contamination free and accessible to integrate into functional structures. We demonstrate this in a particle-on-mirror model system, where >2000 precisely defined nanocavities display a consistent plasmonic response with minimized interstructure variability. Through fabricating arrays of emitter-coupled nanocavities, we further highlight the integration opportunities offered by our contact printing.

INTRODUCTION

Nanoparticles, efficiently formed with tailored structure, composition, and functionalization through bottom-up synthesis, provide unique properties superior to their top-down fabricated counterparts (*1*, *2*). To harness these features for functional nanodevices, individual particles need to be integrated into deterministic designs. To this end, various directed assembly techniques have been developed, where external forces or local chemical and physical cues guide precise particle placements. Examples include optical (*3*), magnetic (*4*) and electrostatic (*5*, *6*) trapping, DNA-mediated patterning (*7*, *8*), dielectrophoretic positioning (*9*, *10*), and capillary assembly (*11*–*13*). However, as these techniques rely on specific particle characteristics and surface treatments, they are incompatible with arbitrary systems and often lack high-throughput processing. Interfacing to the underlying surface for device integration is another challenge, as surface modification, damage, and contamination are often inevitable. Thus, an approach for scalable, precise patterning of nanoparticles into diverse and pristine structures over large areas is still lacking.

To address this need, we present nanoparticle contact printing, a two-step technique through which particles are patterned on diverse surfaces with high fidelity, positional accuracy, and uniformity. In the first step, we leverage the processing flexibility offered by capillary assembly to achieve single-particle spatial ordering (Fig. 1A). In this step, capillary forces, which are insensitive to particle type, selectively immobilize nanoparticles into topographically defined target sites. Although capillary assembly allows positioning of diverse materials (*14*), it on its own does not allow for facile integration with functional devices and systems. The technique relies on wet processing that can damage or introduce contaminants to the receiving surfaces. Moreover, the assembled particles are often left partially embedded in the template after positioning, making them inaccessible for further integration into active structures. To eliminate particle-template contact, thermal removal of the polymeric templates has been shown (*15*). However, the high temperatures needed can hinder applications that use temperature-sensitive nanoparticles and substrates. We alleviate these limitations through our second step, in which we dry-transfer our patterned particles onto a desired surface (Fig. 1A).

Nanoparticle transfer is driven by a differential interfacial adhesion to the target relative to the template. However, given the nanoscale dimensions and lack of conformal contact, adhesive interactions experienced by individual nanoparticles are often insufficiently small, leading to low and unreliable transfer yields. We address this challenge by simultaneously engineering the particle interfacial interactions with the substrate and template to realize a reliable, high-yield, and versatile transfer through a single dry contact-and-release step. This is in contrast to the conventional approaches where improving the transfer yield has relied on modifying the receiving surface with polymer adhesive layers (*11*) or thin liquid films (*16*, *17*). Other techniques have used a sacrificial template material to promote particle release upon its solvent-assisted removal (*18*). These techniques, however, can cause damage, introduce contaminants, change properties, and alter surfaces. In this work, we eliminate the need for these mediations. Using gold nanocubes as an example, we demonstrate clean and scalable patterning on diverse substrates with >95% transfer yield, <50-nm positional accuracy, and minimized interparticle variability. Using a nanoparticle-on-mirror (NPoM) system, we further probe and present the device integration opportunities offered.

RESULTS

High-yield dry nanoparticle contact printing with interfacial engineering

Figure 1 shows an example application of our contact printing technique, fabricating uniform 50 × 50 array of ~55-nm gold nanocubes. First, the nanocubes were assembled onto a polydimethylsiloxane

[1]Department of Chemical Engineering, Massachusetts Institute of Technology, Cambridge, MA 02139, USA. [2]Department of Electrical Engineering and Computer Science, Massachusetts Institute of Technology, Cambridge, MA 02139, USA.
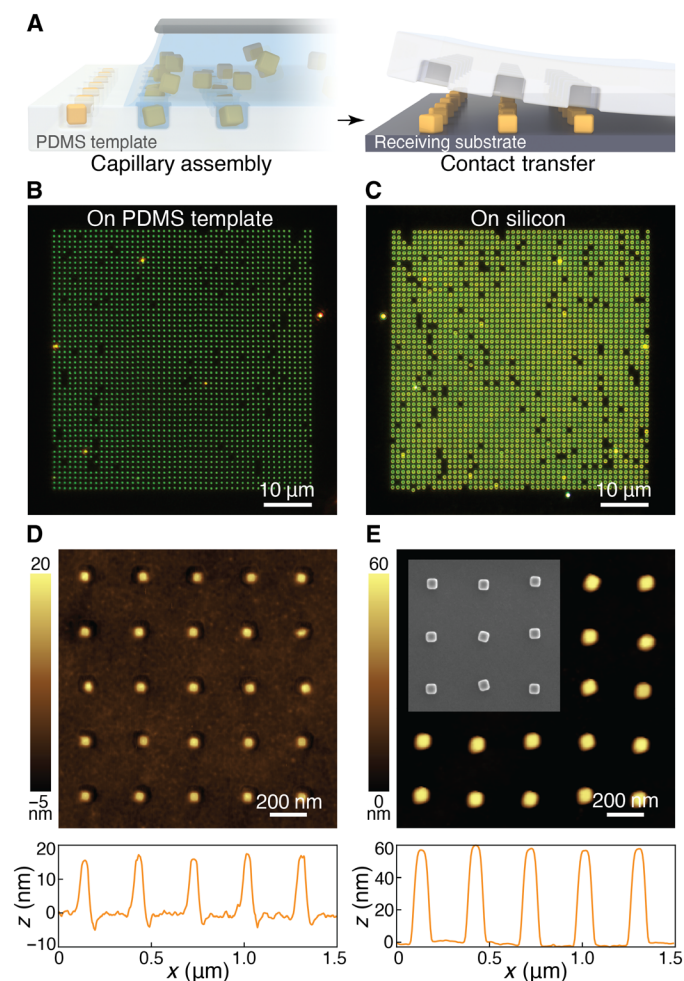*Corresponding author. Email: fniroui@mit.edu

Fig. 1. Nanoparticle contact printing for precise, scalable, and pristine particle patterning. (**A**) Schematic of the printing process: Nanoparticles are positioned onto a PDMS topographical template using capillary assembly, followed by their dry contact transfer onto a receiving substrate. (**B**) Dark-field image of a representative 50 × 50 array of ~55-nm gold nanocubes assembled onto a PDMS template. (**C**) Dark-field image of the same nanocube array after contact transfer onto a silicon substrate. (**D**) AFM image of gold nanocubes assembled onto PDMS template with the height profile showing particle protrusion above the template surface. (**E**) AFM image and height profile after transfer onto silicon surface. The inset shows a scanning electron microscope (SEM) image of the corresponding cubes at the same scale.

(PDMS) topographical template (Fig. 1B) and then dry-transferred onto a silicon substrate with 97% transfer yield (Fig. 1C). Atomic force microscope (AFM) images in Fig. 1 (D and E) reveal the ordered structures achieved. The corresponding fabrication process is detailed in fig. S1.

This reliable and high-yield transfer is realized by controlling the particle-template interfacial adhesion relative to that of the particle-substrate interface. In the absence of solvent or chemical mediations, these interactions are largely dominated by the van der Waals forces. The extent of these interactions depends on the inherent dielectric properties of the interacting surfaces, their separation distance, and the contact area (19). To accommodate transfer of diverse particles to arbitrary substrates, the template-particle adhesion needs to remain low. Thus, we have selected PDMS as the assembly template

material for its well-understood low surface energy (20). Concurrently, intimate nanoscale contact between the particle and the target is needed to maximize the surface adhesive interactions. At the macroscale, this requires a conformal contact between the template and the target substrate. We promoted this macroscopic contact by removing the template from its hard glass backing after assembly and attaching it to a flexible polyethylene terephthalate (PET) film. The flexibility allows the template and target surfaces to closely conform without additional pressure and facilitates their controlled delamination with a steady interfacial release speed, allowing for transfer yields as high as 85%.

We, however, observed a large variation in the transfer yield, with some as low as 3%. We attribute this variation to inhomogeneities in the nanoscale contact between the individual particles and the substrate. To address this, we increased the transfer temperature to enhance the local conformal contact. We expect that the elevated temperature facilitates the rearrangements of the thin surfactant coating around the nanoparticle, enabling it to more uniformly conform to the substrate, thus improving the particle-substrate adhesion. In addition, it is known that adhesion to PDMS reduces with increase in temperature (21, 22), which will assist the particle transfer. As a result, we demonstrated a notable improvement in the single-particle transfer with increasing temperature, reaching >99% yield at 75°C (Fig. 2A). Aside from improved yield, inter- and intrasample variabilities in transfer are also minimized.

This optimized yield is simultaneously and critically assisted by lowering the particle-template adhesion through template engineering, where we reduce the nanoparticle contact area with the template relative to that formed with the target. We modify the contact area by modulating the particle protrusion out of the template. By changing template depth, protrusion heights in the range of 4 to 31 nm were achieved, as characterized in the AFM images of fig. S2. With increasing protrusion, a larger interfacial energy difference becomes available to induce the transfer as the contact to the PDMS is reduced. This trend is theoretically approximated using the Lifshitz model in text S1. By increasing the protrusion, we were able to increase the transfer yield from ~0.1 to >95% (Fig. 2B). Despite an improved transfer yield, increasing protrusion adversely affects the assembly as a shallower template reduces the likelihood of nanoparticle immobilization (12). Thus, optimizing the overall fabrication yield requires this trade-off to be addressed. For the nanocubes in this study, we identified 20-nm protrusion to be most suitable (fig. S3).

The importance of interfacial contact area is further evident in Fig. 2C where a higher transfer yield is achieved for structures with increasing number of nanoparticle-building units. However, as the transfer temperature is elevated to 75°C, the improved particle-substrate adhesion leads to consistent near-unity yields for all samples regardless of their number of constituent particles.

Reliable integration into versatile functional structures

Through our precise engineering of the interfacial interactions, we achieve contact printing without solvent mediation, surface treatments, sacrificial layers or excess applied pressure. Thus, nanoparticle integration onto diverse surfaces and materials can be accommodated in our approach, even those prone to degradation. In Fig. 3A, we demonstrate transfer of 50 × 50 gold nanocube arrays onto a semiconductor (silicon), insulator (silicon dioxide), flexible polymer (PET), metal (template-stripped gold), self-assembled molecular
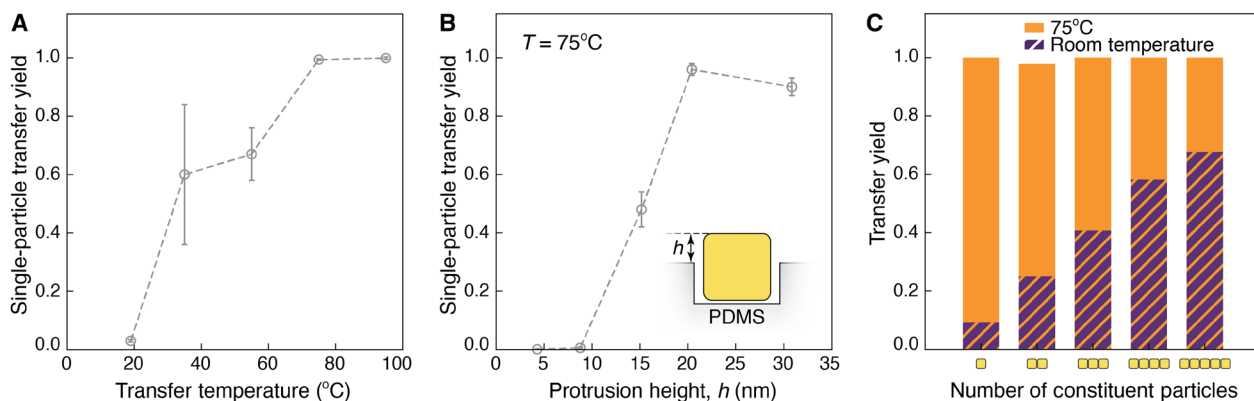
Fig. 2. Improving transfer yield with interfacial engineering. (**A**) Single-particle transfer yield as a function of transfer temperature. (**B**) Single-particle transfer yield as a function of the particle protrusion height (h), at a transfer temperature (T) of 75°C. (**C**) Transfer yield of multiparticle linear structures as a function of the number of constituent nanoparticles at room temperature (purple) and at 75°C (orange). The error bars represent intrasample variations in transfer yields measured for 50-μm by 50-μm arrays of individual nanoparticles across millimeter-scale areas of the sample.

monolayer [biphenyl-4-thiol (BPT)], and two-dimensional material [molybdenum disulfide (MoS_2) monolayer].

As the surfaces are maintained damage and contamination free during transfer, pristine interfaces are available for integration into functional structures and devices. These prospects are evident through the examples of nanometer-thin BPT and MoS_2 layers situated between the contact-printed nanocubes and an underlying gold film. These structures can serve as plasmonic nanocavities for local engineering of light-matter interactions (*23*). Molecular monolayers and two-dimensional materials can be easily damaged, and their intrinsic properties can be altered while being integrated into nanocavities if using conventional lithographic techniques or transfer printing with solvents, sacrificial layers, or surface treatments. With our contact printing approach, a pristine and intact structure is possible. This is characterized in Fig. 3 (B and C) using surface-enhanced Raman spectroscopy, which shows that the Raman signatures of BPT and MoS_2 are preserved under the transferred nanocubes. For BPT, the map reflects the C-H rocking mode integrated at 1080 ± 20 cm^{-1} (*24*), and for MoS_2, the A_{1g} mode is mapped at 395 ± 15 cm^{-1} (*25*).

Printing on diverse surfaces consistently reaches transfer yields >95%. The performance specific to each surface in Fig. 3A is reported in table S1. In the case of MoS_2, a lower yield of 86% is observed. We attribute this lower yield to variations in surface topography introduced as a result of the substrate preparation process, which prevents conformal contact (fig. S4). Improvements are expected through use of a more uniform MoS_2 surface, a customized template geometry, and a more controlled template aligning strategy.

Because we have optimized our process for high-yield transfer to diverse surfaces, our overall fabrication yield is dominated by the assembly yield of nanoparticles into our PDMS template. Hence, the missing particles in Fig. 3A primarily stem from incomplete assembly, which can be optimized independent of the transfer. Aside from changes in the assembly process parameters and template (*12*, *14*), we have demonstrated that sequential assembly can also be used to heal the unfilled defect sites and improve yield (fig. S5).

In addition to high fabrication yields, our process results in accurate particle placement due to the absence of solvents or excess pressure. Analysis of more than 13,000 nanoparticles printed on silicon gives a mean position accuracy of 43 nm (Fig. 3D), which exceeds previously reported transfer printing values (*11*, *18*). We

determine the placement accuracy by measuring the distance by which each particle in an array is offset from its designated position as defined by the template. The annotated dark-field image in fig. S6A helps visualize this approach. As the patterned region becomes smaller, such as the 5-μm by 5-μm array shown in fig. S6B, a higher precision accuracy of 11 nm is measured, approaching that reported for capillary assembly without a transfer printing step (*15*).

The precision afforded by our approach also enables fabrication of more complex patterns, composed of individual nanoparticles or their ensembles. Examples of particles forming the letters of alphabet and linear connected structures on silicon are shown in Fig. 3 (E and F, respectively). Our approach can also be extended to nanoparticles with other geometries and material compositions. We demonstrate this in Fig. 3G where we have contact printed arrays of gold nanospheres and silver nanocubes with >90% transfer yield. The performance specific to each sample is reported in table S1.

Consistent plasmonic response in an NPoM array

Aside from scalable, precise, and versatile processing, integration of nanoparticles into functional structures and devices requires uniform, repeatable performance across fabricated arrays. Here, we use the NPoM plasmonic resonator to probe the uniformity resulting from our fabrication process. In this structure, a nanoparticle is placed on a metallic film, separated by a thin dielectric spacer. The resulting nanocavity strongly confines light and displays plasmon modes highly sensitive to the constituent materials and geometry (*23*, *26*), with subnanometer variations detectable (*27–29*). In addition to their diverse applications in nanophotonics (*30–34*), sensing (*28*), and catalysis (*35*, *36*), these nanocavities can serve as powerful probes of the nanoscale structures. Here, we used them to characterize the uniformity of our contact printing.

To fabricate an array of NPoM nanocavities with our contact printing approach, gold nanocubes were assembled and transferred onto a template-stripped gold film. The surfactant layer capping the nanocubes, visible in the transmission electron microscope (TEM) image of fig. S7, defines the dielectric spacer. See Materials and Methods for a detailed description of substrate preparation. Figure 4A shows characteristics scattering spectra of individual nanoparticles with the inset showing the corresponding dark-field image of a 70×40 nanoparticle array. The fabricated structures display a highly
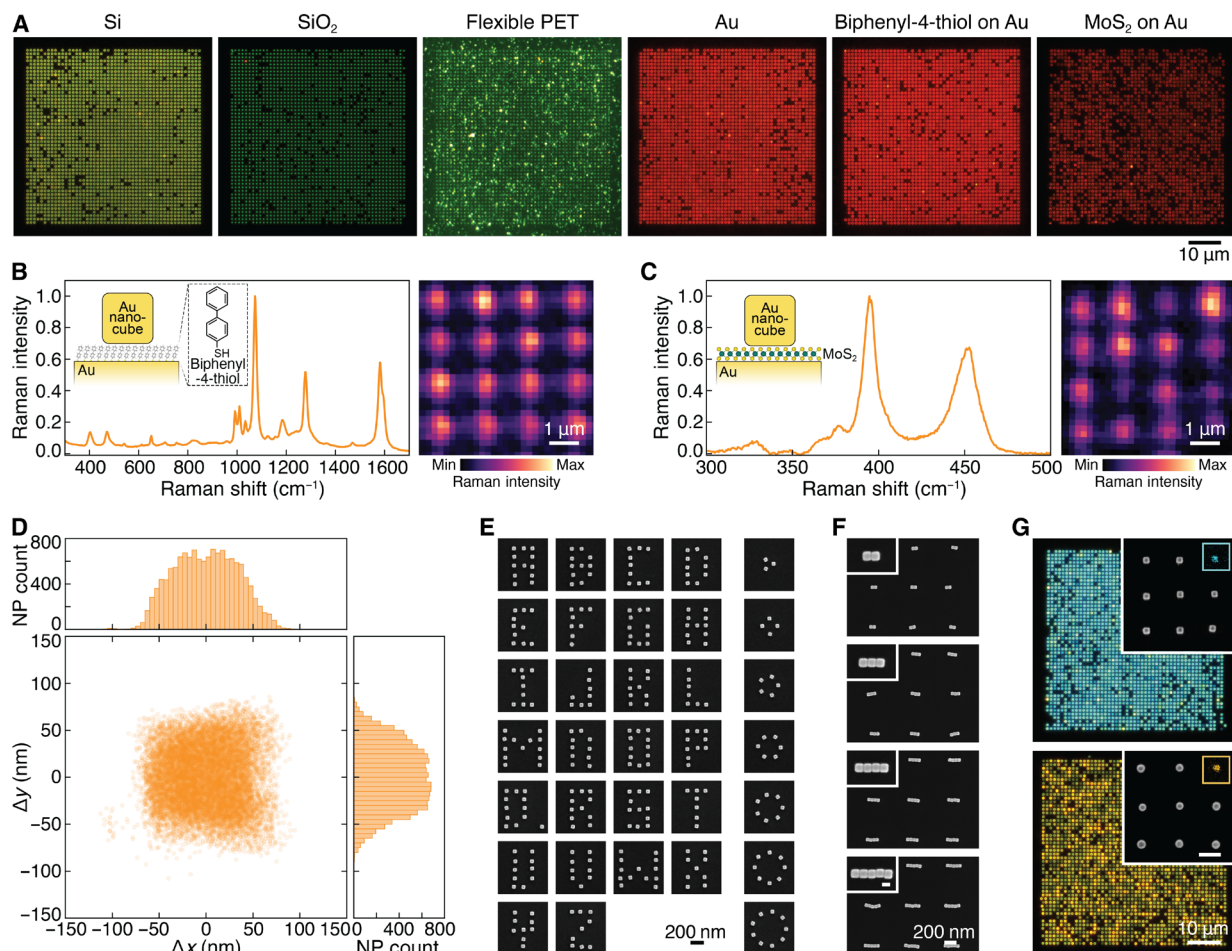
Fig. 3. Versatile integration with diverse surfaces and designs. (**A**) Dark-field images of gold nanocube arrays contact printed onto pristine Si, SiO$_2$, flexible PET, template-stripped gold film, BPT monolayer on gold, and exfoliated MoS$_2$ monolayer on gold. In the case of PET, the background scattering comes from the rough surface. Representative surface-enhanced Raman spectroscopy spectra and map for (**B**) BPT and (**C**) MoS$_2$ samples are shown. The BPT map is integrated at 1080 ± 20 cm^{-1} (C-H rocking mode) and MoS$_2$ at 395 ± 15 cm^{-1} (A$_{1g}$ mode). (**D**) Distribution of individual nanoparticle lateral offset relative to their designated position as defined by the template, shown for 13,610 nanoparticles, represents a mean placement accuracy of 43 nm upon transfer. Nanoparticles can also be patterned into more complex designs. SEM examples show (**E**) individual nanocubes forming the letters of alphabet and (**F**) linear structures with controlled number of particle-building units, all printed onto silicon. The scale bar on the inset of (F) corresponds to 50 nm. (**G**) Dark-field images of silver nanocube (top) and gold nanosphere (bottom) arrays contact printed onto Si. The inset shows representative SEM images of an assembled array and the energy-dispersive x-ray mapping of an individual Ag (blue) and Au (yellow) nanoparticle. The scale bar on the inset is 200 nm.

consistent optical response, evident in the uniform scattering spectra measured for >2400 densely patterned NPoMs with an average resonance of 666 ± 8 nm (Fig. 4B). This is a notable improvement over the conventionally fabricated NPoM structures shown in Fig. 4 (C and D). These structures are formed by drop-casting the nanoparticles onto the gold film, resulting in a random and low-density distribution of structures, visible in the inset of Fig. 4C. The spectra show a broad distribution in resonance wavelength, intensity, and spectral shape (Fig. 4C). The resonance distribution of 681 ± 22 nm (Fig. 4D) is indicative of the presence of a much larger internanocavity variability compared to the contact-printed counterparts.

This improved repeatability in the optical response can be attributed to the structural uniformity achieved with our contact printing technique. Through template design, we reduce the nanoparticle size variation and shape polydispersity inherent to the colloidal synthesis. As depicted in the TEM analyses in figs. S8 and S9, the contact-printed nanocubes display a tighter structural dispersion, in both shape and size, compared to that observed for drop-casted particles. The ~60% decrease in size and corner rounding variations for contact-printed particles results from our approach preferentially mediating assembly and transfer of nanocubes over the bipyramid and rod by-products. In addition, replacing direct wet assembly on the target substrate by dry contact printing helps avoid surface contamination, resulting in a well-defined nanogap width based on the uniform nanocube surfactant coating (fig. S7). In the drop-casted counterparts, excess surfactant from the colloidal solution can accumulate on the surface, introducing additional inhomogeneities.

Consequently, the use of contact printing allows us to achieve uniform plasmonic response due to improved shape, size, and nanogap uniformity. Sensitivity analysis and finite-difference time-domain simulations, presented in text S2, indicate that the small
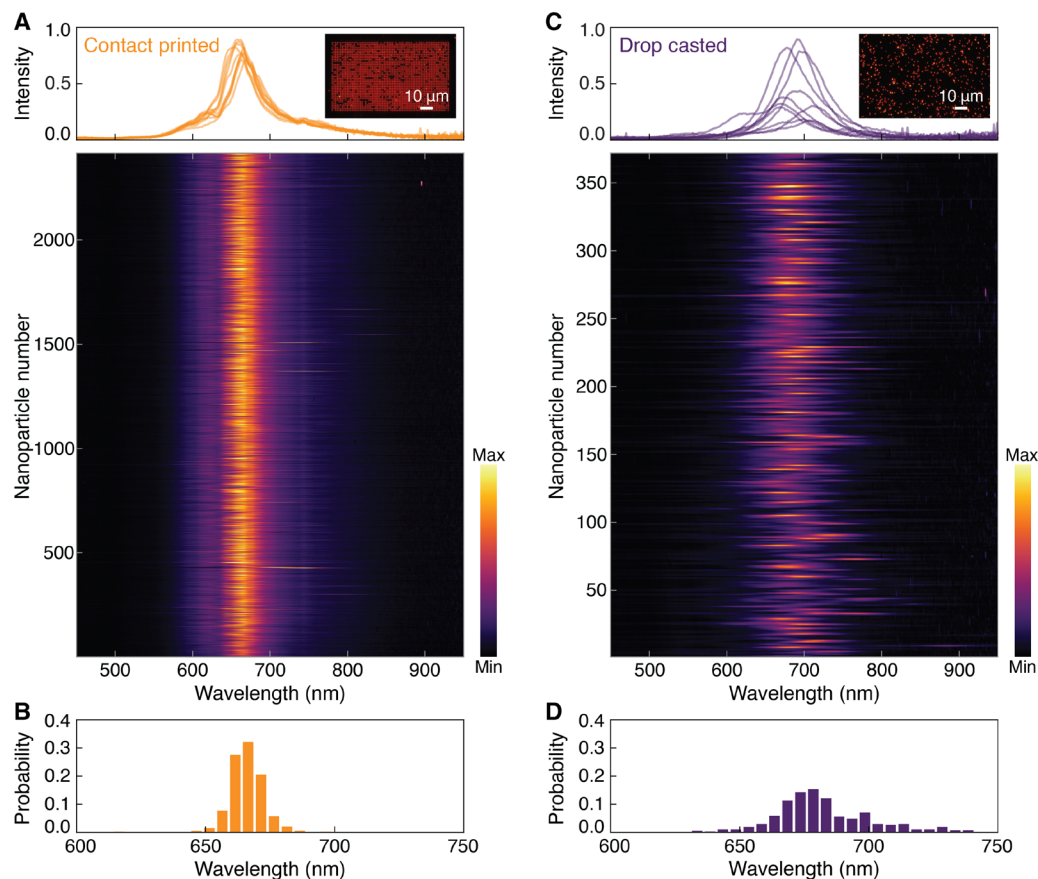
Fig. 4. Uniform spectral response in a contact-printed particle-on-mirror nanocavity array. (**A** and **B**) Contact-printed NPoM nanocavities are compared against (**C** and **D**) the drop-casted structures. For each case, 10 random single-particle spectra are shown on the top plot, with dark-field image as inset. Dark-field scattering spectra of all sampled nanocubes are shown in the waterfall plots. A tighter resonance peak distribution is observed for (B) 2417 contacted-printed nanoparticles (666 ± 8 nm), as compared to (D) 371 drop-casted particles (681 ± 22 nm).

remaining variability is due to the experimentally measured size and shape dispersity of the nanocubes combined with a minute gap variation of ~1.6 Å.

Scalable integration of nanocavity-enhanced molecular emission

To highlight the integration opportunities offered by our contact printing approach, we further demonstrated arrays of emitter-coupled NPoM nanocavities with fluorescent dye molecules embedded in the nanogap (Fig. 5A). These plasmonic structures with small mode volumes and concentrated optical fields can finely engineer the emitters' electromagnetic environment to tune their optical response (*23*). By controlling the coupling strength through cavity design, previous studies have successfully demonstrated notable enhancements in spontaneous emission (*30–32*) and produced strong coupling (*33*, *34*). To reach the necessary subnanometer control over structure and pristine nanogaps with intact emitters, bottom-up fabricated NPoM constructs are uniquely suitable. However, the use of drop-casted nanoparticles has prevented the fabrication of large arrays of uniform cavities, restricting high-throughput studies and practical applications. In addition, the need for pristine interfaces and the potential chemical instability of the molecular emitters limit use of conventional printing approaches that are mediated by

solvents and high temperatures. However, the precise, scalable and dry processing offered by our contact printing can alleviate these limitations.

Figure 5B shows arrays of >1900 nanocavities fabricated using contact-printed gold nanocubes and Atto-594 dye molecules embedded in a polymer spacer, 8 nm in thickness. Here, the nanogap is designed such that the resonance overlaps with the dye absorption and emission spectra (Fig. 5C). The resulting nanocavities yield an average fluorescence enhancement of 123-fold compared to a control sample of dye molecules on glass, measured under a 589-nm pulsed laser excitation. Related calculations are described in text S3.

We further performed correlative optical measurements on a 5 × 5 subarray of the contact-printed nanocavities, characterizing the scattering spectral response, in addition to the fluorescence response and its temporal dynamics. The structural uniformity resulting from our contact printing gives a tightly distributed plasmonic resonance of 598 ± 4 nm, measured through dark-field scattering spectroscopy (Fig. 5D). The dye-coupled cavities emit at 611 ± 3 nm (Fig. 5E) with a fluorescence decay time of 38 ± 15 ps (Fig. 5F). This decay time shows a notable decrease compared to the 2.6-ns lifetime of the dye molecule on glass, corresponding to an average 77× enhancement in the spontaneous emission rate. The ability to perform correlative measurements over large arrays of deterministically fabricated

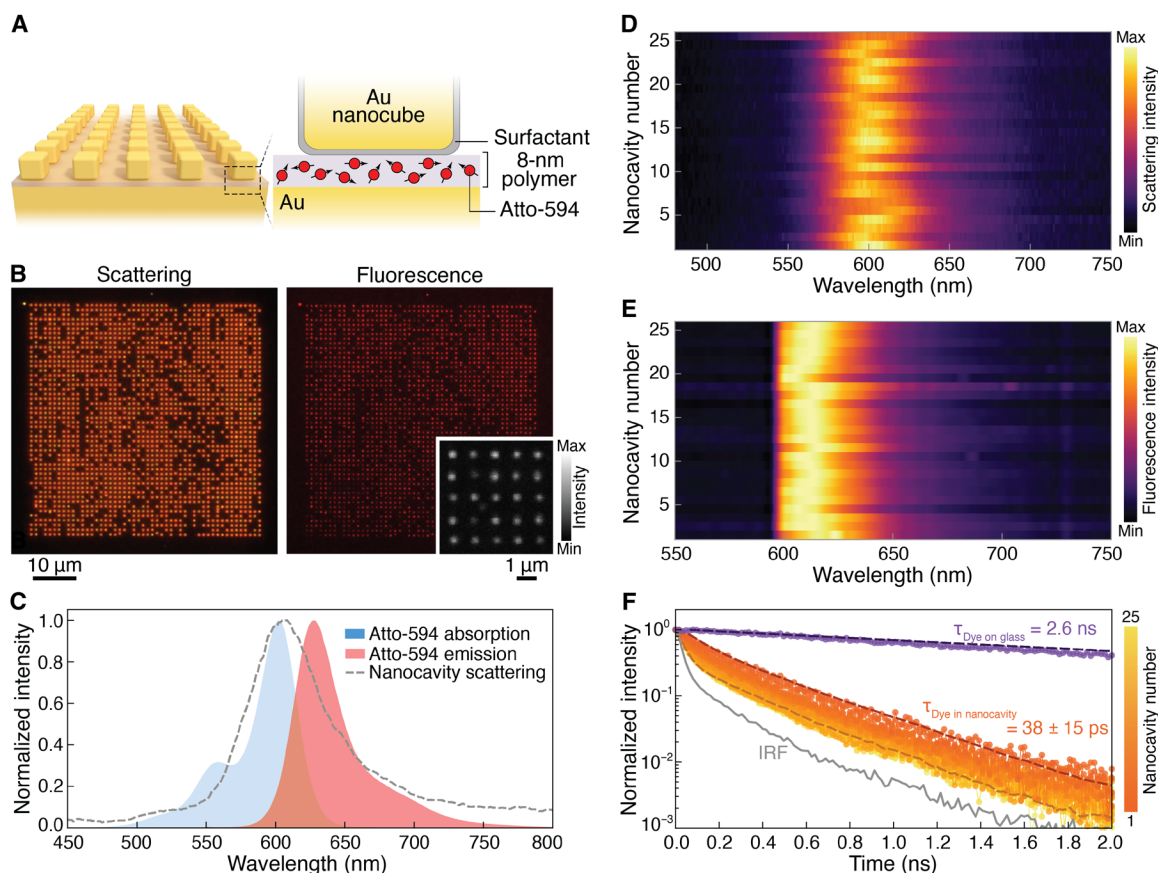**Fig. 5. Emitter-integrated plasmonic nanocavity arrays using nanoparticle contact printing.** (**A**) Schematic of the particle-on-mirror nanocavity composed of a nanocube on a gold film separated by an 8-nm polymer spacer containing Atto-594 dye molecules. (**B**) Dark-field (left) and corresponding fluorescence (right) images of a representative array of emitter-embedded nanocavities with the inset showing the fluorescence intensity map of a 5 × 5 subarray. (**C**) The absorption and emission spectra of Atto-594 dye overlapped with a representative scattering spectrum of the nanocavity. Correlated (**D**) scattering spectra, (**E**) fluorescence spectra, and (**F**) time-resolve fluorescence decay for the array of 5 × 5 nanocavities shown in the inset of (B). The latter also includes the instrument response function (IRF) and the response of the dye on glass. The experimental results are fitted to extract the lifetimes (τ) (dashed curves). The dashed curves on top of the measured fluorescence decay of individual cavities show the fitting to the fast and slow bounds of the measured decay times. The emission is measured through a 600-nm longpass filter.

nanocavities highlights the prospects of our technique for enabling high-throughput statistical studies and integration into functional devices and systems.

DISCUSSION

In summary, we have developed a technique for precise, scalable, and pristine patterning of nanoparticles with single-particle resolution. Core to our approach is engineering of nanoscale interfacial interactions, through which capillary-assembled particles can be printed onto diverse surfaces without solvents, surface treatments, or sacrificial release layers at near unity yield. Thus, unlike conventional nanoparticle placement strategies, inherent particle properties can be retained, and surfaces maintained clean during patterning, with interfaces suitable for integration into functional nanoscale devices. The fabricated structures can be achieved with high-throughput and minimized variability, resulting in uniform and predictable performance, as we demonstrated using a sensitive plasmonic NPoM design. Leveraging these attributes, we further highlighted the ability to integrate these structures into more complex systems through an example of emitter-coupled nanocavities.

As both the capillary assembly and transfer printing are versatile, our technique has the prospect to accommodate diverse material systems beyond those immediately studied in this work. Patterns with arbitrary designs and composition and heterostructures with diverse properties can be fabricated. Large-area and sequential printing can also be envisioned through future developments to enable more complex, multicomponent, and even nonplanar structures with spatially controlled design and composition. In addition, scalable and versatile processing combined with control over surfaces and interfaces at the single-particle level provides access to otherwise hard-to-probe features, simultaneously allowing high-throughput studies. As a result, beyond enhancing our fundamental understanding of the nanoscale, new emerging applications can be realized in fields including plasmonics, nanoelectronics, optoelectronics, and nanoelectromechanical systems.

MATERIALS AND METHODS
Substrate preparation
Silicon and silicon dioxide substrates were cleaned in acetone, followed by boiling isopropanol prior to transfer printing. The flexible

125-µm-thick PET sample was cleaned in boiling isopropanol before use. To prepare template-stripped gold substrates, first, ~150 nm of gold was thermally evaporated onto a clean silicon wafer. The gold on silicon was then bonded to a glass backing substrate using an optical adhesive (NOA-61, Norland Products). Once cured under ultraviolet light, the glass substrate was detached from the silicon, peeling with it the gold film to reveal its ultrasmooth surface (<1-nm root mean square roughness). The BPT on gold sample was prepared by immersing a template-stripped gold substrate in a 1 mM solution of BPT (MilliporeSigma) in anhydrous ethanol for 22 hours. After growth, the substrate was briefly sonicated and rinsed in ethanol to remove excess molecules and then dried under a stream of nitrogen. The MoS_2 on gold sample was prepared by exfoliation from a natural MoS_2 crystal (SPI Supplies) adhered to an ultraviolet-release tape (Ultron Systems) using a template-stripped gold surface (37, 38). During this process, the MoS_2 on tape was brought into contact with the template-stripped gold and placed on a 130°C hotplate for 2 min. The sample was then removed from the hotplate and the tape was slowly peeled. The resulting MoS_2 consisted of millimeter-scale monolayer domains, in addition to regions of few-layer and bulk MoS_2 as shown in fig. S4.

The Atto-594 on gold sample with a polymer spacer was prepared using a previously reported layer-by-layer coating process (30, 31). A template-stripped gold substrate was immersed in a cationic solution of 3 mM poly(allylamine hydrochloride) (PAH; MilliporeSigma) and 1 M NaCl for 5 min immediately upon stripping. Then, the sample was immersed in an anionic solution of 3 mM poly(styrene sulfonate) (PSS; MilliporeSigma) and 1 M NaCl for 5 min. The sample was rinsed in a 1 M NaCl solution between the successive polymer layer coatings. To form a spacer that is 8 nm in thickness, seven layers of the polymer films were formed on gold, terminated by PAH. After rinsing in deionized (DI) water and drying under nitrogen, the sample was immersed in a 10 µM aqueous solution of Atto-594 (MilliporeSigma) for 20 min, followed by a thorough rinse in DI water. Control samples were prepared using the same procedure on glass substrate.

Gold nanocube synthesis
Gold nanocubes were synthesized using a previously reported procedure (39). All chemicals used were purchased from MilliporeSigma, with the exception of cetyltrimethylammonium chloride (CTAC), which was purchased from Tokyo Chemical Industry. Briefly, ~10-nm CTAC-capped gold nanosphere seeds were prepared and used to nucleate the growth of gold nanocubes. Nanocubes were realized by selectively capping the (100) facets with bromine ions. By varying the bromine, seed, and CTAC concentrations, cubes of different sizes could be realized with minimal corner rounding. The specific nanocubes used in this work have a size of ~55 nm, with a 15-nm rounding as synthesized. TEM analysis of the synthesized cubes is presented in fig. S9. Our synthesis results in a nanocube yield of ~91%, without post-synthetic purification. The primary by-products of this synthesis are nanobipyramids and nanorods (39), which, as discussed in the as discussed in the Results Section, can be selected against with careful template design (fig. S8). For optimal assembly outcome, the surfactants used during synthesis were exchanged for an aqueous mixture of 0.1 weight % (wt %) of Triton X-45 (MilliporeSigma) and 1 mM sodium dodecyl sulfate (SDS; MilliporeSigma).

Gold nanospheres and silver nanocubes
Gold nanospheres (80 nm in diameter) and silver nanocubes (55 nm in size) were purchased from nanoComposix. Similar to gold nanocubes, the citrate-capped gold nanospheres and polyvinyl pyrrolidone–capped silver nanocubes underwent a surfactant exchange with a mixture of 0.1 wt % of Triton X-45 and 1 mM SDS in DI water before assembly.

Nanoparticle contact printing
The fabrication process is schematically shown in fig. S1 and described below.
Mold fabrication
The mold was fabricated by electron-beam lithographic patterning of hydrogen silsesquioxane (HSQ; Dow Corning) on silicon substrate. HSQ was spin-coated onto a plasma-treated Si substrate with the desired thickness. The thickness was selected in accordance with the template depth needed. HSQ was then exposed by an electron beam at 125-keV acceleration with a 2-nA beam current and a dose of 16,000 µC/cm^2 (FLS-125, Elionix). For studying single-particle transfer, square traps, 85 nm in size, were used for the gold and silver nanocubes, and 120-nm circular traps were used for the gold nanospheres. The exposed sample was developed in a solution of 1 wt % of NaOH and 4 wt % of NaCl for 60 s, then rinsed in DI water, and dried under nitrogen.
Template fabrication
Hard PDMS (hPDMS) templates were replicated from the patterned HSQ molds. Oxygen plasma-treated molds were functionalized with 1*H*,1*H*,2*H*,2*H*-perfluorodecyltriethoxysilane (MilliporeSigma) to prevent adhesion to the PDMS template. Prepolymer mixture of hPDMS, consisting of 3.4-g VDT-731 (vinylmethylsiloxane-dimethylsiloxane, Gelest), 18 µl of SIP6831.2 (platinum catalyst, Gelest), 5 µl of 2,4,6,8-tetramethyl-2,4,6,8-tetravinylcyclotetrasiloxane (MilliporeSigma), and 1.0-g HMS-301 (methylhydrosiloxane-dimethylsiloxane copolymer, Gelest) (40), was thoroughly mixed. The mixture was immediately spin-coated onto the fluorinated mold at 3000 rpm for 30 s. The mold was then brought into contact with a soft PDMS (Sylgard 184) film on a glass backing. The stack was cured at 75°C for 14 hours. Once cured, the PDMS was peeled from the mold exposing the topographical template.
Capillary assembly
Capillary assembly was performed using a home-built setup, where a drop (~50 µl) of colloidal nanoparticle suspension was sandwiched between the template and a blade moving at 2 µm/s. A temperature of 35°C above the dew point was used for the assembly. The receding contact angle during assembly was measured to be 46°.
Contact transfer
To promote macroscale conformal contact between the template and receiving substrate, the template with the assembled nanoparticles was released from the hard glass backing and attached to a flexible 125-µm-thick PET film. The template was then brought into contact with the receiving substrate without excess applied pressure. After heating the sample on a hotplate for 5 min at the desired temperature, the template was slowly delaminated at an interfacial release speed of ~10 µm/s using a stepper motor to mechanically lift the PET. To transfer nanoparticles to the MoS_2 sample, the assembled nanoparticles were aligned to the monolayer region before printing. To accommodate this, the nanoparticles were moved to the region of interest on the substrate and brought into contact while imaging through the PET backing under a dark-field microscope.

Optical measurements
Raman and optical scattering measurements were performed with a Horiba XploRA system using a 100×, numerical aperture (NA) = 0.9

dark-field objective. Raman samples were collected under a 785-nm laser excitation, with incident power in the range of 4.8 to 12 mW depending on the sample. The dark-field scattering spectra were recorded with a CytoViva hyperspectral imaging system, with illumination from an unpolarized tungsten source. The collected scattering spectra were first intensity corrected using a calibrated scattering standard. They were then background corrected by subtracting the spectrum of the gold substrate without any nanoparticles.

Fluorescence measurements were performed with a custom-built confocal microscope using a 100×, NA = 0.85 objective. The output of a supercontinuum laser (SuperK Extreme, NKT Photonics) was filtered through an acousto-optic tunable filter (AOTF) (SpectraK Dual, NKT Photonics) and centered at 589 nm with a pulse repetition rate of 40 MHz. The output of the AOTF was fiber-coupled to a single-mode photonic crystal fiber and collimated with an achromatic fiber collimator (C40FC-A, Thorlabs) for a beam diameter of ~7.4 mm. The laser output was filtered through a 586/15-nm bandpass filter and directed to the back aperture of the objective with a 561-nm dichroic filter (Di01-R561, Semrock). The laser spot size on the sample surface was measured to be ~700 nm. Emitted light from the sample was passed through a 600-nm longpass filter to remove the residual excitation laser before measurements. The fluorescence spectra were collected using a monochromator (SP2300, Princeton Instruments) and a thermoelectrically cooled charge-coupled device (PIXIS 100, Princeton Instruments). The time-resolved florescence measurements were performed using a single-photon avalanche photodiode (MPD PDM Series, 50 µm) connected to a time-correlated single-photon counting module (PicoHarp 300, PicoQuant). All measurements were conducted at an average laser power of 8 nW incident on the sample. This power lies in the linear regime of the emission response as shown in the fig. S12. The decay lifetimes were determined by fitting a biexponential function convolved with the instrument response function (IRF) to the measured data. The IRF was determined from the emission of an Allura Red solution. The accuracy of the fast component of the biexponential decay is limited by the ~64-ps full width at half maximum of the IRF.

SUPPLEMENTARY MATERIALS
Supplementary material for this article is available at https://science.org/doi/10.1126/sciadv.abq4869

REFERENCES AND NOTES

1. P. Yang, J. Zheng, Y. Xu, Q. Zhang, L. Jiang, Colloidal synthesis and applications of plasmonic metal nanoparticles. *Adv. Mater.* **28**, 10508–10517 (2016).
2. M. Liu, N. Yazdani, M. Yarema, M. Jansen, V. Wood, E. H. Sargent, Colloidal quantum dot electronics. *Nat. Electron.* **4**, 548–558 (2021).
3. A. S. Urban, A. A. Lutich, F. D. Stefani, J. Feldmann, Laser printing single gold nanoparticles. *Nano Lett.* **10**, 4794–4798 (2010).
4. A. F. Demirörs, P. P. Pillai, B. Kowalczyk, B. A. Grzybowski, Colloidal assembly directed by virtual magnetic moulds. *Nature* **503**, 99–103 (2013).
5. M. Krishnan, N. Mojarad, P. Kukura, V. Sandoghdar, Geometry-induced electrostatic trapping of nanometric objects in a fluid. *Nature* **467**, 692–695 (2010).
6. S. Fringes, C. Schwemmer, C. D. Rawlings, A. W. Knoll, Deterministic deposition of nanoparticles with sub-10 nm resolution. *Nano Lett.* **19**, 8855–8861 (2019).
7. Q.-Y. Lin, J. A. Mason, Z. Li, W. Zhou, M. N. O'Brien, K. A. Brown, M. R. Jones, S. Butun, B. Lee, V. P. Dravid, K. Aydin, C. A. Mirkin, Building superlattices from individual nanoparticles via template-confined DNA-mediated assembly. *Science* **359**, 669–672 (2018).
8. W. Zhou, Z. Liu, Z. Huang, H. Lin, D. Samanta, Q.-Y. Lin, K. Aydin, C. A. Mirkin, Device-quality reconfigurable metamaterials from shape-directed nanocrystal assembly. *Proc. Natl. Acad. Sci. U.S.A.* **117**, 21052–21057 (2020).
9. A. Barik, X. Chen, S.-H. Oh, Ultralow-power electronic trapping of nanoparticles with sub-10 nm gold nanogap electrodes. *Nano Lett.* **16**, 6317–6324 (2016).
10. F. Niroui, M. Saravanapavanantham, J. Han, J. J. Patil, T. M. Swager, J. H. Lang, V. Bulović, Hybrid approach to fabricate uniform and active molecular junctions. *Nano Lett.* **21**, 1606–1612 (2021).
11. T. Kraus, L. Malaquin, H. Schmid, W. Riess, N. D. Spencer, H. Wolf, Nanoparticle printing with single-particle resolution. *Nat. Nanotechnol.* **2**, 570–576 (2007).
12. V. Flauraud, M. Mastrangeli, G. D. Bernasconi, J. Butet, D. T. L. Alexander, E. Shahrabi, O. J. F. Martin, J. Brugger, Nanoscale topographical control of capillary assembly of nanoparticles. *Nat. Nanotechnol.* **12**, 73–80 (2016).
13. S. Ni, H. Wolf, L. Isa, Programmable assembly of hybrid nanoclusters. *Langmuir* **34**, 2481–2488 (2018).
14. S. Ni, L. Isa, H. Wolf, Capillary assembly as a tool for the heterogeneous integration of micro- and nanoscale objects. *Soft Matter* **14**, 2978–2995 (2018).
15. F. Holzner, C. Kuemin, P. Paul, J. L. Hedrick, H. Wolf, N. D. Spencer, U. Duerig, A. W. Knoll, Directed placement of gold nanorods using a removable template for guided assembly. *Nano Lett.* **11**, 3957–3962 (2011).
16. A. Cerf, G. Molnár, C. Vieu, Novel approach for the assembly of highly efficient SERS substrates. *ACS Appl. Mater. Interfaces* **1**, 2544–2550 (2009).
17. H. Agrawal, E. C. Garnett, Nanocube imprint lithography. *ACS Nano* **14**, 11009–11016 (2020).
18. J. B. Lee, H. Walker, Y. Li, T. W. Nam, A. Rakovich, R. Sapienza, Y. S. Jung, Y. S. Nam, S. A. Maier, E. Cortés, Template dissolution interfacial patterning of single colloids for nanoelectrochemistry and nanosensing. *ACS Nano* **14**, 17693–17703 (2020).
19. J. Israelachvili, *Intermolecular and Surface Forces* 107–132 (Elsevier, 2012).
20. A. Carlson, A. M. Bowen, Y. Huang, R. G. Nuzzo, J. A. Rogers, Transfer printing techniques for materials assembly and micro/nanodevice fabrication. *Adv. Mater.* **24**, 5284–5318 (2012).
21. H. Awada, O. Noel, T. Hamieh, Y. Kazzi, M. Brogly, Contributions of chemical and mechanical surface properties and temperature effect on the adhesion at the nanoscale. *Thin Solid Films* **519**, 3690–3694 (2011).
22. S.-H. Hur, D. Y. Khang, C. Kocabas, J. A. Rogers, Nanotransfer printing by use of noncovalent surface forces: Applications to thin-film transistors that use single-walled carbon nanotube networks and semiconducting polymers. *Appl. Phys. Lett.* **85**, 5730–5732 (2004).
23. J. J. Baumberg, J. Aizpurua, M. H. Mikkelsen, D. R. Smith, Extreme nanophotonics from ultrathin metallic gaps. *Nat. Mater.* **18**, 668–678 (2019).
24. F. Benz, C. Tserkezis, L. O. Herrmann, B. de Nijs, A. Sanders, D. O. Sigle, L. Pukenas, S. D. Evans, J. Aizpurua, J. J. Baumberg, Nanooptics of molecular-shunted plasmonic nanojunctions. *Nano Lett.* **15**, 669–674 (2015).
25. W. Chen, S. Zhang, M. Kang, W. Liu, Z. Ou, Y. Li, Y. Zhang, Z. Guan, H. Xu, Probing the limits of plasmonic enhancement using a two-dimensional atomic crystal probe. *Light Sci. Appl.* **7**, 56 (2018).
26. R. Chikkaraddy, X. Zheng, F. Benz, L. J. Brooks, B. de Nijs, C. Carnegie, M. E. Kleemann, J. Mertens, R. W. Bowman, G. A. E. Vandenbosch, V. V. Moshchalkov, J. J. Baumberg, How ultranarrow gap symmetries control plasmonic nanocavity modes: From cubes to spheres in the nanoparticle-on-mirror. *ACS Photonics* **4**, 469–475 (2017).
27. J. J. Mock, R. T. Hill, A. Degiron, S. Zauscher, A. Chilkoti, D. R. Smith, Distance-dependent plasmon resonant coupling between a gold nanoparticle and gold film. *Nano Lett.* **8**, 2245–2252 (2008).
28. W. Chen, S. Zhang, Q. Deng, H. Xu, Probing of sub-picometer vertical differential resolutions using cavity plasmons. *Nat. Commun.* **9**, 801 (2018).
29. C. Readman, B. de Nijs, I. Szabó, A. Demetriadou, R. Greenhalgh, C. Durkan, E. Rosta, O. A. Scherman, J. J. Baumberg, Anomalously large spectral shifts near the quantum tunnelling limit in plasmonic rulers with subatomic resolution. *Nano Lett.* **19**, 2051–2058 (2019).
30. G. M. Akselrod, C. Argyropoulos, T. B. Hoang, C. Ciracì, C. Fang, J. Huang, D. R. Smith, M. H. Mikkelsen, Probing the mechanisms of large Purcell enhancement in plasmonic nanoantennas. *Nat. Photonics* **8**, 835–840 (2014).
31. A. J. Traverso, G. Yang, J. Huang, M. H. Mikkelsen, T. Peyronel, T. G. Tiecke, Low-loss, centimeter-scale plasmonic metasurface for ultrafast optoelectronics. *Optica* **8**, 202–207 (2021).
32. T. B. Hoang, G. M. Akselrod, M. H. Mikkelsen, Ultrafast room-temperature single photon emission from quantum dots coupled to plasmonic nanocavities. *Nano Lett.* **16**, 270–275 (2016).
33. R. Chikkaraddy, B. de Nijs, F. Benz, S. J. Barrow, O. A. Scherman, E. Rosta, A. Demetriadou, P. Fox, O. Hess, J. J. Baumberg, Single-molecule strong coupling at room temperature in plasmonic nanocavities. *Nature* **535**, 127–130 (2016).
34. M. E. Kleemann, R. Chikkaraddy, E. M. Alexeev, D. Kos, C. Carnegie, W. Deacon, A. C. de Pury, C. Große, B. de Nijs, J. Mertens, A. I. Tartakovskii, J. J. Baumberg, Strong-coupling of WSe$_2$ in ultra-compact plasmonic nanocavities at room temperature. *Nat. Commun.* **8**, 1296 (2017).
35. D. O. Sigle, L. Zhang, S. Ithurria, B. Dubertret, J. J. Baumberg, Ultrathin CdSe in plasmonic nanogaps for enhanced photocatalytic water splitting. *J. Phys. Chem. Lett.* **6**, 1099–1103 (2015).
36. B. de Nijs, F. Benz, S. J. Barrow, D. O. Sigle, R. Chikkaraddy, A. Palma, C. Carnegie, M. Kamp, R. Sundararaman, P. Narang, O. A. Scherman, J. J. Baumberg, Plasmonic tunnel junctions for single-molecule redox chemistry. *Nat. Commun.* **8**, 994 (2017).

37. Y. Huang, Y. H. Pan, R. Yang, L. H. Bao, L. Meng, H. L. Luo, Y. Q. Cai, G. D. Liu, W. J. Zhao, Z. Zhou, L. M. Wu, Z. L. Zhu, M. Huang, L. W. Liu, L. Liu, P. Cheng, K. H. Wu, S. B. Tian, C. Z. Gu, Y. G. Shi, Y. F. Guo, Z. G. Cheng, J. P. Hu, L. Zhao, G. H. Yang, E. Sutter, P. Sutter, Y. L. Wang, W. Ji, X. J. Zhou, H. J. Gao, Universal mechanical exfoliation of large-area 2D crystals. *Nat. Commun.* **11**, 2453 (2020).

38. M. Heyl, D. Burmeister, T. Schultz, S. Pallasch, G. Ligorio, N. Koch, E. J. W. List-Kratochvil, Thermally activated gold-mediated transition metal dichalcogenide exfoliation and a unique gold-mediated transfer. *Phys. Status Solidi RRL* **14**, 2000408 (2020).

39. J. E. Park, Y. Lee, J. M. Nam, Precisely shaped, uniformly formed gold nanocubes with ultrahigh reproducibility in single-particle scattering and surface-enhanced Raman scattering. *Nano Lett.* **18**, 6475–6482 (2018).

40. S. Ni, J. Leemann, H. Wolf, L. Isa, Insights into mechanisms of capillary assembly. *Faraday Discuss.* **181**, 225–242 (2015).

41. R. Zhao, T. Koschny, E. N. Economou, C. M. Soukoulis, Repulsive Casimir forces with finite-thickness slabs. *Phys. Rev. B* **83**, 075108 (2011).

42. A. Lambrecht, I. Pirozhenko, L. Duraffourg, P. Andreucci, The Casimir effect for silicon and gold slabs. *Europhys. Lett.* **77**, 44006 (2007).

43. P. J. van Zwol, G. Palasantzas, Repulsive Casimir forces between solid materials with high-refractive-index intervening liquids. *Phys. Rev. A* **81**, 062502 (2010).

44. C. J. Drummond, D. Y. C. Chan, van der Waals interaction, surface free energies, and contact angles: Dispersive polymers and liquids. *Langmuir* **13**, 3890–3895 (1997).

45. P. B. Johnson, R. W. Christy, Optical constants of the noble metals. *Phys. Rev. B* **6**, 4370–4379 (1972).